Chinese Journal of Catalysis 88 (2026) 259–268

available at www.sciencedirect.com

ScienceDirect

journal homepage: www.sciencedirect.com/journal/chinese-journal-of-catalysis

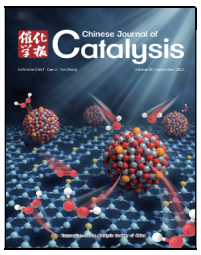

Article

Direct electrosynthesis of ammonia from nitrate reduction using atomically precise carbonyl-rich metal clusters in neutral media

Miao Wang [a,b,1], Tianyu Shen [a,1], Heng Zhou [c,1], Shuaikang Yang [a], Fengkun Hao [b], Chaohui Wang [b], Mohan Kumar [d], Zuoxiu Tie [a,*], Shuangming Chen [c,*], Zhanxi Fan [b,*], Zhong Jin [a,*]

[a] *State Key Laboratory of Coordination Chemistry, MOE Key Laboratory of Mesoscopic Chemistry, MOE Key Laboratory of High Performance Polymer Materials and Technology, Jiangsu Key Laboratory of Green Energy Catalysis and Intelligent Chemical Engineering, Suzhou Key Laboratory of Green Intelligent Manufacturing of New Energy Materials and Devices, Tianchang New Materials and Energy Technologies Research Center, Institute of Green Chemistry and Engineering, School of Chemistry and Chemical Engineering, Nanjing University, Nanjing 210023, Jiangsu, China*

[b] *Department of Chemistry, Hong Kong Branch of National Precious Metals Material Engineering Research Center (NPMM), Hong Kong Institute for Clean Energy, City University of Hong Kong, Kowloon, Hong Kong 999077, China*

[c] *National Synchrotron Radiation Laboratory, Chinese Academy of Sciences Center for Excellence in Nanoscience, University of Science and Technology of China, Hefei 230029, Anhui, China*

[d] *Department of Chemistry, PES Institute of Technology and Management, Shivamogga 577204, Karnataka, India*

ARTICLE INFO

Article history:
Received 12 November 2025
Accepted 5 February 2026
Available online 5 September 2026

Keywords:
Carbonyl-enriched metal clusters
Atomically precise architectures
Electrochemical nitrate reduction
Ammonia electrosynthesis
Density functional theory calculations

ABSTRACT

Atomically precise metal clusters, as an advantageous platform for investigating the active site architectures and catalytic mechanisms, remain largely underexplored. Here, we demonstrate that carbonyl-rich metal clusters (CRMC) serve as exemplary electrocatalytic platforms, enabling highly efficient and selective electroreduction of nitrate to ammonia under neutral aqueous conditions. To establish a comprehensive structure-performance correlation, we systematically investigated an array of diverse carbonyl-rich metal clusters, including Co_2-CRMC, Co_4-CRMC, Ru_3-CRMC, Fe_2-CRMC, Fe_3-CRMC, Mo-CRMC, W-CRMC and Mn_2-CRMC. Among them, Co_2-CRMC electrode delivered exceptional performance, with a Faradaic efficiency of 97.2% and an ammonia yield rate of 150.5 mmol h^{-1} $g^{-1}_{cat.}$, while Co_4-CRMC electrode achieved a Faradaic efficiency of 98.7% and a yield rate of 129.2 mmol h^{-1} $g^{-1}_{cat.}$. Theoretical calculations and mechanism studies reveal that the high catalytic activity stems from enhanced NO_3^- adsorption and a reduced energy barrier for the *NO hydrogenation steps. Furthermore, electrostatic potential analyses highlight the critical role of metal-carbonyl ligand interactions in optimizing the electronic environment of metal centers, facilitating stronger NO_3^- adsorption. This research offers a profound molecular-level understanding for the design of sophisticated metal-cluster catalysts, opening avenues for efficient nitrogen cycling processes and environmental restoration efforts.

1. Introduction

Ammonia (NH_3) is a cornerstone of industrial chemistry, playing a vital role in nitrogen fertilizer production and

* Corresponding author. E-mail: zxtie@nju.edu.cn (Z. Tie), csmp@ustc.edu.cn (S. Chen), zhanxi.fan@cityu.edu.hk (Z. Fan), zhongjin@nju.edu.cn (Z. Jin).
[1] Contributed equally to this work.
This work was supported by the National Natural Science Foundation of China (U25A20628, 22561160129, 22479074, 22475096), the Equipment Pre-Research and Ministry of Education Joint Fund (8091B02052407), the Fundamental Research Program Key Project of Jiangsu Province (BK20253008), the Science and Technology Major Project of Jiangsu Province (BG2024013), the Scientific and Technological Achievements Transformation Special Fund of Jiangsu Province (BA2023037), the Academic Degree and Postgraduate Education Reforming Project of Jiangsu Province (JGKT24_C001), the Key Core Technology Open Competition Project of Suzhou City (SYG2024122), the Open Research Fund of Suzhou Laboratory (SZLAB-1308-2024-TS005), the Chenzhou National Sustainable Development Agenda Innovation Demonstration Zone Provincial Special Open Competition Project (2023sfq11, 2025sfq38), and the Fundamental Research Funds for the Central Universities and Nanjing University International Collaboration Initiative (020514380354).
https://doi.org/10.1016/S1872-2067(26)65146-7

emerging as a promising hydrogen-rich energy carrier [1,2]. However, the conventional Haber-Bosch process for NH_3 synthesis operates under extreme conditions of high temperature and pressure, accounting for approximately 1.5% of global energy consumption and 1.0%–2.0% of worldwide CO_2 emissions [3]. Electrochemical NH_3 synthesis offers a sustainable and environmentally friendly alternative to replace the Haber-Bosch process. Nevertheless, the practical application of direct electrocatalytic nitrogen (N_2) reduction reaction (NRR) is hindered by the low solubility of N_2 gas and the high dissociation energy of the N≡N triple bond (941 kJ mol^{-1}) [4–9]. These challenges have spurred interest in the electrocatalytic nitrate reduction reaction (NITRR) as a more efficient route for NH_3 production [10–15]. Nitrate, a highly soluble and lower-energy (204 kJ mol^{-1}) nitrogen source, is not only abundant globally but also a significant environmental pollutant, making its conversion into NH_3 both practical and beneficial for environmental remediation [16]. By leveraging renewable electricity, NITRR transforms harmful nitrates into valuable NH_3, contributing to sustainable nitrogen cycling.

The NITRR process involves the transfer of eight electrons and nine protons ($NO_3^- + 6H_2O + 8e^- \rightarrow NH_3 + 9OH^-$), necessitating a substantial supply of active hydrogen (H*). Insufficient H* availability at active sites often leads to side reactions, reducing Faradaic efficiency (FE) and NH_3 yield [17,18]. Additionally, the competing hydrogen evolution reaction (HER) further complicates the process, as H* recombination into H_2 diverts electrons from NH_3 production. Therefore, designing electrocatalysts with optimized active sites is critical [19,20]. These catalysts must efficiently dissociate water to generate H* while preventing H* recombination, ensuring high NH_3 selectivity and yield. Atomically precise metal clusters, with their well-defined structures, offer a promising platform for studying and optimizing these processes [21,22]. According to the *d*-band center theory, an upshifted *d*-band center strengthens interactions between metal sites and adsorbates, enhancing catalytic activity. Introducing electron-withdrawing functional groups as ligands can modulate the *d*-band center, improving adsorption and proton-coupled electron transfer capabilities [23]. These insights highlight the potential of molecularly engineered metal clusters as high-performance NITRR electrocatalysts, enabling the establishment of intrinsic structure-activity relationships.

Herein, we explore carbonyl-rich metal clusters as a model platform for investigating active site configurations and NITRR mechanisms. We systematically investigate a series of carbonyl-rich metal clusters (CRMC), including Co_2-CRMC, Co_4-CRMC, Ru_3-CRMC, Fe_2-CRMC, Fe_3-CRMC, Mo-CRMC, W-CRMC and Mn_2-CRMC, to elucidate their structure–performance relationships in NITRR. Among them, Co_2-CRMC and Co_4-CRMC clusters exhibit exceptional NH_3 production performance, achieving FEs of ~98.0% in neutral aqueous media. Theoretical calculations and mechanism studies reveal that the high catalytic activity originates from preferential NO_3^- adsorption and lowered energy barriers for the *NO hydrogenation steps. Electrostatic potential (ESP) analyses further demonstrate that carbonyl ligands enhance the nucleophilic properties of metal centers, facilitating NO_3^- adsorption. The findings provide a new paradigm for the study of other coordination-based electrocatalytic systems, such as metal-organic frameworks (MOFs), covalent organic frameworks (COFs), and molecular electrocatalysts [24–29], opening new avenues for sustainable catalysis.

2. Experimental

2.1. Chemicals and materials

All the carbonyl-rich metal clusters investigated in this study were received from Shanghai Aladdin Biochemical Technology Co., Ltd.. Co_2-CRMC (dicobalt octacarbonyl ($Co_2(CO)_8$, 98%)), Co_4-CRMC (tetracobalt dodecacarbonyl ($Co_4(CO)_{12}$, 98%)), Ru_3-CRMC (triruthenium dodecacarbonyl ($Ru_3(CO)_{12}$, 99%)), Fe_2-CRMC (diiron nonacarbonyl ($Fe_2(CO)_9$, 97%)), Fe_3-CRMC (triiron dodecacarbonyl ($Fe_3(CO)_{12}$, 96%)), Mn_2-CRMC (dimanganese decacarbonyl ($Mn_2(CO)_{10}$, 98%)), Mo-CRMC (molybdenum hexacarbonyl ($Mo(CO)_6$, 98%)), and W-CRMC (tungsten hexacarbonyl ($W(CO)_6$, 97%)].

2.2. Material characterizations

The crystalline structures and phase compositions of the samples were analyzed using powder X-ray diffraction (PXRD, Bruker D8 Advance diffractometer) with a Cu K_α (λ = 1.5418 Å) radiation source. Attenuated total reflectance Fourier transform infrared (ATR-FTIR) spectra were measured on a Thermo Fisher Scientific Optics NICOLETIS10 FTIR spectrometer with a Universal ATR accessory in the range of 4000 to 400 cm^{-1}. Field-emission scanning electron microscopy (FE-SEM, FEI Nova Nano-450 instrument) was utilized for morphological and structural characterizations. Transmission electron microscopy (TEM) was conducted using a JEM-2100 instrument. To investigate the detailed surface compositions and valence states of all samples, X-ray photoelectron spectroscopy (XPS) was carried out using a PHI-5000 Versa Probe instrument. The K-edge extended X-ray absorption fine structure spectroscopy (EXAFS) was conducted by the transition mode at the BL14W1 end station in the Shanghai Synchrotron Radiation Facility (SSRF). The acquired EXAFS data were processed and fitted according to standard procedures using the ATHENA module of the IFEFFIT software packages. The ultraviolet-visible (UV-vis) absorbance data were measured using a Shimadzu UV-2600 spectrophotometer.

2.3. Electrocatalytic measurements

For the preparation of working electrodes, a piece of carbon paper (CP, 1 × 1 cm^2) was cleaned using acetone, alcohol, and water, then dried in a vacuum oven at 80 °C. The electrocatalyst ink was created by dispersing 4 mg of the specific sample in a 1:1 mixture of deionized (DI) water and ethanol (900 μL), followed by the addition of 100 μL Nafion. This mixture was ultrasonicated for 30 minutes. Afterward, 100 μL of the electrocatalyst ink was applied to the CP and dried at room temperature. The NITRR measurements were conducted with a

CHI-760E electrochemical workstation at room temperature and ambient pressure using an H-type cell divided by a Nafion-117 proton exchange membrane. A platinum disk electrode (1 × 1 cm^2) served as the counter electrode, while a saturated Ag/AgCl electrode served as the reference electrode. For industrially relevant current density performances in NITRR, the custom-made flow cell was employed. The electrolyte was purged with high-purity Ar gas flow for 5 min prior to the NITRR measurements. Linear sweep voltammetry (LSV) tests were conducted at a scan rate of 5 mV s^{-1}. After each electrolysis operation, the electrolyte was analyzed using UV-vis absorption spectrophotometry, as described below. All applied potentials were calibrated against the reversible hydrogen electrode (RHE) using the following equation:

$$E\ (vs.\ \text{RHE}) = E\ (vs.\ \text{Ag/AgCl}) + 0.1989 + 0.059 \times \text{pH} \quad (1)$$

3. Results and discussion

3.1. Structural and compositional characterizations

Carbonyl-rich metal clusters, such as Co_2-CRMC and Co_4-CRMC, serve as exemplary models for studying metal-carbon interactions in coordination chemistry. The crystalline structure of Co_2-CRMC features a dimeric arrangement, with two cobalt atoms bridged by carbonyl ligands (Fig. 1(a)). Co_2-CRMC adopts a symmetrical configuration, comprising both terminal and bridging carbonyl groups, which impart distinct electronic properties. In contrast, Co_4-CRMC exhibits a tetranuclear cobalt core, showcasing greater coordination complexity and electronic delocalization (Fig. 1(b)). These structural features not only highlight the stabilizing role of carbonyl ligands but also underscore their potential for catalytic applications in neutral aqueous environments. PXRD analyses confirmed the phase purity of both clusters, with no detectable impurities (Fig. 1(c)). FTIR spectroscopy provided further insights into their vibrational characteristics. Both clusters displayed distinct absorption bands: terminal carbonyl ligands appeared at higher frequencies (~2044 cm^{-1}), while bridging carbonyls were observed at lower frequencies (~1891 cm^{-1}) (Fig. 1(d)). These bands reflect the electron density distribution and the essence of Co-Co interactions.

XPS analyses of the cobalt carbonyl clusters offer valuable insights into their phase characteristics and oxidation states. Survey XPS spectra demonstrate the existence of Co, C, O ele-

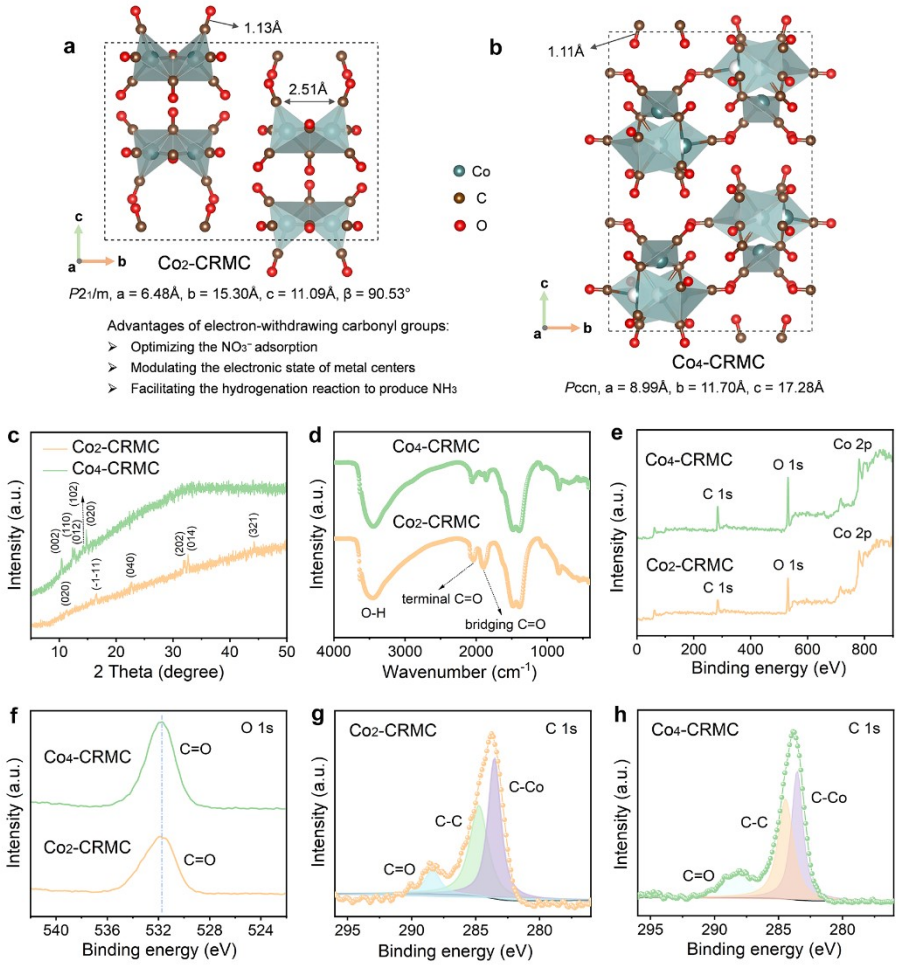

Fig. 1. Structural and compositional characterizations. Crystal structures of carbonyl-enriched Co_2-CRMC (a) and Co_4-CRMC clusters (b). PXRD patterns (c) and FTIR spectra (d) of two carbonyl-rich cobalt clusters. Survey XPS spectra (e) and high-resolution XPS spectra (f) at O 1*s* level of two cobalt clusters. High-resolution XPS spectra at C 1*s* level for Co_2-CRMC (g) and Co_4-CRMC clusters (h).

ments in the Co_2-CRMC and Co_4-CRMC clusters (Fig. 1(e)). The O 1*s* spectra exhibited a peak at 531.7 eV, corresponding to C=O functional groups (Fig. 1(f)) [30], while the C 1*s* spectra showed a peak at 288.3 eV, attributed to carbon atoms in C=O bonds (Figs. 1(g)–(h)) [31,32]. These findings confirm the linkage of carbonyl groups in both clusters. SEM images of these clusters revealed the morphology of microcrystal aggregates (Fig. S1). Elemental mapping confirmed the homogeneous distribution of Co, C, and O within both samples. TEM further elucidated the morphological features of the clusters (Fig. S2).

High-resolution XPS spectra at Co 2*p* level of Co_2-CRMC and Co_4-CRMC clusters displayed peaks at 781.6 eV ($2p_{3/2}$) and 797.4 eV ($2p_{1/2}$), characteristic of Co^{2+} species, along with satellite peaks at 786.8 and 803.1 eV (Fig. 2(a)) [33–35]. X-ray absorption fine structure (XAFS) analyses at the Co K-edge provided insights into the local coordination and electronic structure. The adsorption edge positions of Co_2-CRMC and Co_4-CRMC clusters were similar to that of CoO, indicating a divalent state for Co atoms in the clusters (Fig. 2(b)). Fourier-transform EXAFS fitting results identified two main peaks: the first shell (Co-C coordination) at ~1.56 Å and the second shell (Co-O coordination) at ~2.70–2.73 Å (Fig. 2(c)). Quantitative analysis revealed coordination numbers of ~5 for Co_2-CRMC and ~3.5 for Co_4-CRMC in the first shell (Figs. 2(d)–(f), Table S1). The difference between Co K-edge wavelet transformation of two cobalt clusters and other reference samples distinctly corroborated that the first shell is Co-C coordination instead of Co-O (Figs. 2(g)–(j)).

3.2. Electrocatalytic NITRR measurements

The electrocatalytic NITRR performances of two carbonyl-rich cobalt cluster electrodes, Co_2-CRMC and Co_4-CRMC, were evaluated in a H-cell system under neutral conditions. LSV curves recorded in electrolytes with varying nitrate concentrations and without nitrate ions are shown in Figs. 3(a), (d) and Figs. S3, S4, respectively, indicating the distinct electrochemical activities for each catalyst towards nitrate species. The NITRR tests were performed in two electrolytes: a 0.1 mol L^{-1} Na_2SO_4–0.1 mol L^{-1} KNO_3 mixed solution (applied potential: –0.6 to –0.9 V *vs.* RHE) and a 0.5 mol L^{-1} KNO_3 solution (applied potential: –0.4 to –0.7 V *vs.* RHE). Since nitrate (NO_3^-) is both the reactant and a key conducting species, its rapid consumption by the highly active electrocatalysts during long-term stability tests would otherwise lead to a continuous drop in solution conductivity. This would increase the cell resistance and

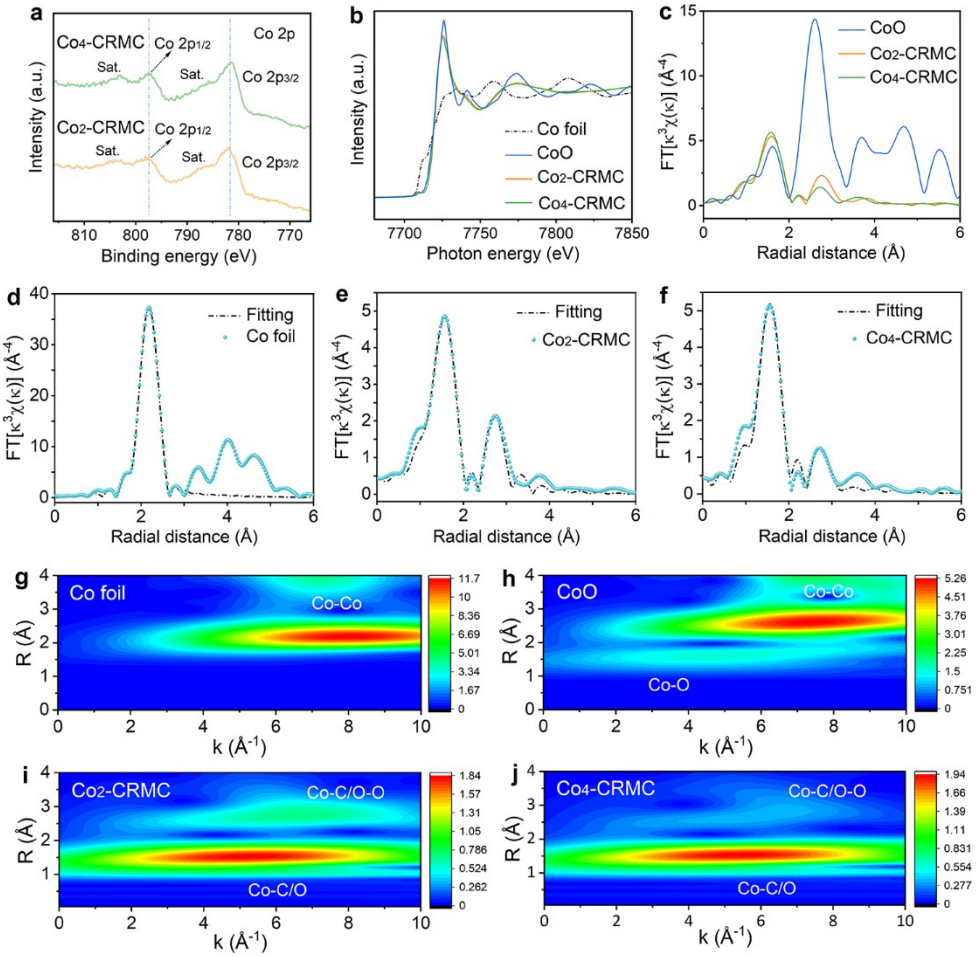

Fig. 2. Fine structure characterizations. (a) XPS spectra at Co 2*p* level for carbonyl-enriched Co_2-CRMC and Co_4-CRMC clusters. Co K-edge XANES (b) and EXAFS (c) spectra of two cobalt clusters along with other reference samples. (d–f) Co K-edge EXAFS fitting curves of two cobalt cluster samples. (g–j) Co K-edge wavelet transformations of two cobalt clusters along with other reference samples.

voltage, complicating the following stability assessment in low-concentration nitrate electrolyte. The inert sodium sulfate provides a constant and high ionic strength, ensuring stable electrolyte conductivity throughout the experiment and allowing us to focus on the catalyst's performance analysis. Time-resolved current density measurements over 30 min at different overpotentials revealed a monotonic increase in current density with more negative potentials (Fig. S5). In the 0.1 M Na_2SO_4–0.1 mol L^{-1} KNO_3 mixed electrolyte, both electrodes demonstrated exceptional performances for selective NH_3 synthesis (Figs. 3(b), (c)). The Co_2-CRMC electrode achieved a maximum Faradaic efficiency (FE) of 97.2% with an NH_3 yield rate of 150.5 mmol h^{-1} $g^{-1}_{cat.}$, while the Co_4-CRMC electrode reached an FE of 98.7% with a yield rate of 129.2 mmol h^{-1} $g^{-1}_{cat.}$. In the 0.5 mol L^{-1} KNO_3 electrolyte, the performances slightly declined (Figs. 3(e), (f)). The Co_2-CRMC electrode exhibited an FE of 87.7% and a yield rate of 225.1 mmol h^{-1} $g^{-1}_{cat.}$ at –0.5 V (*vs.* RHE), whereas the Co_4-CRMC electrode achieved an FE of 94.3% and a yield rate of 138.1 mmol h^{-1} $g^{-1}_{cat.}$ at –0.4 V (*vs.* RHE).

The product analyses of nitrogen-containing species in the NITRR on Co_2-CRMC and Co_4-CRMC electrodes at various potentials are quantitatively summarized in Figs. S6–S8. Using a mixed electrolyte of 0.1 mol L^{-1} Na_2SO_4 and 0.1 mol L^{-1} KNO_3, the detection of only minimal nitrite (NO_2^-) byproducts demonstrates high selectivity toward the electrochemical conversion of nitrate to ammonia. A comparison of Co_2-CRMC and Co_4-CRMC with representative electrocatalysts reported in prior studies (Fig. S9) indicates that both electrodes achieve competitive FE_{NH3} values compared to many prior works [36–51]. To verify the origin of the ammonia product, ^{15}N-labeled nitrate ($Na^{15}NO_3$, 98.3% enrichment) was utilized as a tracer. The resulting ^1H NMR spectrum (Fig. S10) displayed the characteristic doublet of $^{15}NH_4^+$ in the post-reaction electrolyte, which contrasts with the triplet pattern observed for $^{14}NH_4^+$ when using nitrate at natural abundance. These distinct isotopic signals confirm that the electrochemically generated ammonia originates from the reduction of nitrate, rather than from adventitious nitrogen contaminants.

A comparative assessment of electrochemical surface area (ECSA) was performed to examine the intrinsic catalytic features of the Co_2-CRMC and Co_4-CRMC electrodes. Cyclic volt-

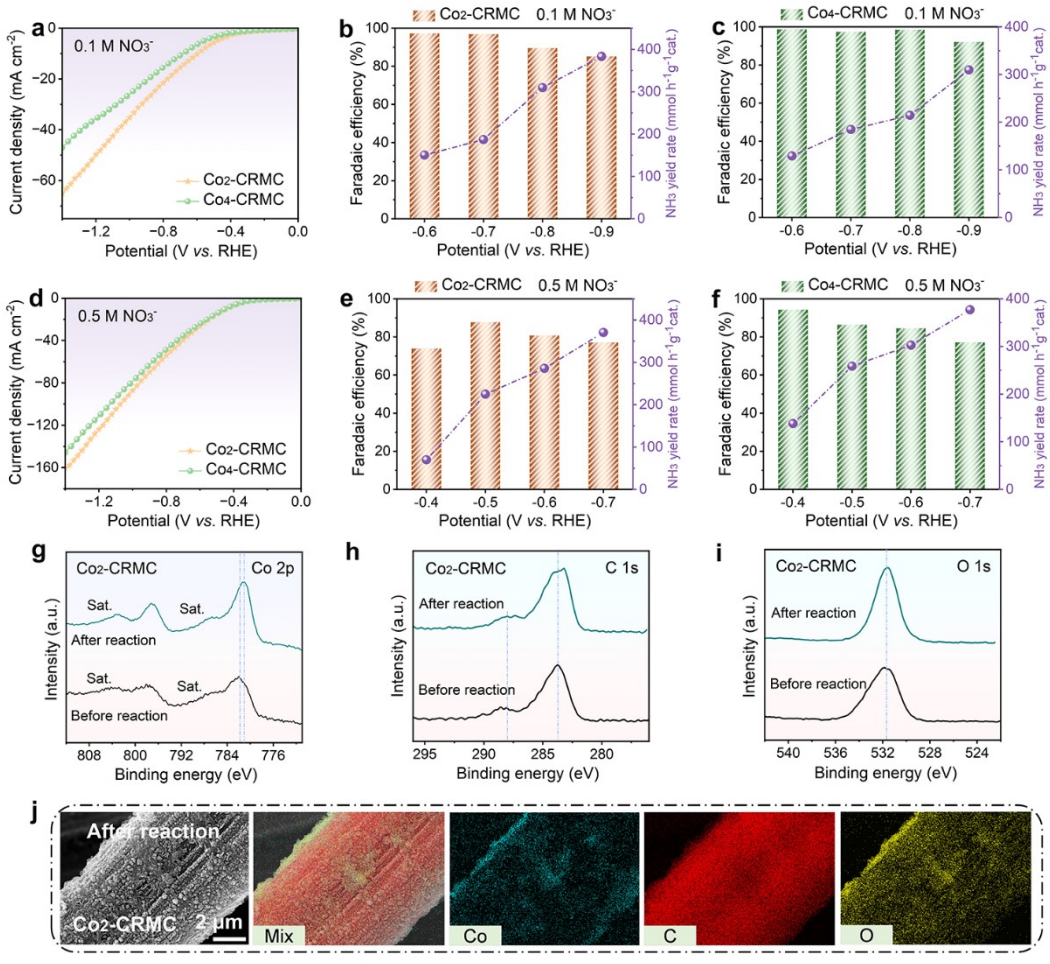

Fig. 3. Electrocatalytic NITRR activities of two carbonyl-rich cobalt cluster electrodes. (a) LSV curves of the two samples tested in 0.1 mol L^{-1} Na_2SO_4–0.1 mol L^{-1} KNO_3 mixed electrolyte. FE values and NH_3 yield rates of Co_2-CRMC (b) and Co_4-CRMC (c) electrodes for the NITRR. (d) LSV curves of the two samples tested in 0.5 mol L^{-1} KNO_3 electrolyte. FE values and NH_3 yield rates of Co_2-CRMC (e) and Co_4-CRMC (f) electrodes for the NITRR. XPS spectra at Co 2*p* level (g), C 1*s* (h), and O 1*s* (i) levels of Co_2-CRMC electrode before and after the NITRR process. (j) Typical SEM image and elemental mappings of Co_2-CRMC clusters supported on carbon paper (CP) after the NITRR process.

ammetry (CV) was carried out between −0.45 and −0.55 V (*vs.* Ag/AgCl), and the double-layer capacitance (C_{dl}) was derived from the linear relationship between the current density difference at −0.50 V and the scan rate. As illustrated in Fig. S11, the calculated C_{dl} for Co_4-CRMC (0.40 mF cm^{-2}) exceeds that of Co_2-CRMC (0.27 mF cm^{-2}), indicating a moderately larger electrochemical active surface area of Co_4-CRMC than that of Co_2-CRMC. This higher capacitance implies greater accessibility of active sites for accommodating nitrate reduction intermediates. Electrochemical impedance spectroscopy (EIS) further distinguished the charge-transfer behaviors of the two electrodes (Fig. S12). The Nyquist plots demonstrate that Co_2-CRMC presents a lower charge-transfer resistance (R_{ct}) relative to Co_4-CRMC, pointing to more facile electron transfer kinetics within the Co_2-CRMC.

Ex-situ XPS analyses of the Co_2-CRMC electrode before and after the NITRR process revealed a slight negative shift in the Co 2*p* binding energy, indicating a reduction in the cobalt oxidation state under negative bias (Fig. 3(g)). The C 1*s* and O 1*s* XPS spectra confirmed the persistence of carbonyl groups after the electrocatalytic reaction testing (Figs. 3(h), (i)). Additionally, SEM and elemental mapping images showed minimal morphological changes in the Co_2-CRMC electrode post-reaction, to some extent, confirming its structural stability (Fig. 3(j)). Notably, we experimentally observed a subtle structural reconstruction in two types of cobalt-based metal clusters (*i.e.*, Co_2-CRMC and Co_4-CRMC), which may optimize the interaction of electrocatalyst with nitrate ions and reaction intermediates synergistically, leading to enhanced catalytic activity and ammonia selectivity.

3.3. Fine structure characterizations and electrocatalytic tests of other carbonyl-rich metal clusters

The Ru K-edge X-ray absorption near-edge structure (XANES) spectra of Ru_3-CRMC, RuO_2, and Ru foil revealed similar adsorption edge positions, suggesting that the Ru in Ru_3-CRMC is close to a tetravalent state (Fig. S13(a)). In the *R*-space plot, the first peak for Ru_3-CRMC appeared at 1.36 Å, corresponding to Ru-C coordination in the first shell, while the first peak for RuO_2 was observed at 1.50 Å, attributed to Ru-O coordination, as displayed in Fig. S13(b). Fourier-transform EXAFS fitting results indicated that the first coordination shell of Ru_3-CRMC consists of approximately four Ru-C bonds with an average bond length of 1.87 Å (Fig. S13(c), Fig. S14, and Table S2). The difference between Ru K-edge wavelet transformation of Ru_3-CRMC and RuO_2 distinctly corroborates that the first shell of Ru_3-CRMC is Ru-C coordination instead of Ru-O (Figs. S13(d), (e)).

The electrocatalytic performances of a series of other carbonyl-rich metal cluster electrodes (Ru, Fe, Mn, Mo, and W) were also evaluated for the NITRR under ambient conditions. Their crystal structures are illustrated in Figs. S15–S19. LSV curves in 0.5 mol L^{-1} KNO_3 solution demonstrated varying activities among the electrodes, with Ru_3-CRMC exhibiting the highest response to nitrate species (Figs. S13(f) and (h)). Time-resolved current density measurements over a 0.5-h period for the Ru_3-CRMC electrode are shown in Fig. S20. The ammonia production performances of the electrodes generally followed the order: Ru_3-CRMC > Fe_3-CRMC > Fe_2-CRMC > Mo-CRMC > W-CRMC > Mn_2-CRMC (Figs. S13(g) and (i))). Notably, the Ru_3-CRMC electrode achieved a Faradaic efficiency (FE) of 84.9% at –0.9 V (*vs.* RHE) with an NH_3 yield rate of 245.9 mmol h^{-1} g$^{-1}_{cat.}$, outperforming Fe_3-CRMC (79.2% FE) and Fe_2-CRMC (78.3% FE). The long-term NITRR stability tests over 40000 s confirmed the robustness of Ru_3-CRMC electrode, with no significant decline in current density or FE (Fig. S13(j)).

3.4. Theoretical calculations and mechanism studies

Density functional theory (DFT) calculations were employed to explore the role of carbonyl groups in modulating the electronic structure of the metal center in the Co_2-CRMC cluster [52]. Projected density of states (PDOS) analysis of *NO_3 adsorption revealed strong interactions between the Co 3*d* orbitals and NO_3^-, with the Co 3*d* orbitals positioned near the Fermi level (E_f), indicating enhanced catalytic activity (Fig. 4(a)). The significant orbital overlap between Co 3*d* and NO_3^- orbitals ensures stable adsorption, facilitating the subsequent NITRR process. Electrostatic potential (ESP) analysis further highlighted the influence of carbonyl groups, showing a highly positive ESP value (25.01 kcal mol^{-1}) at the Co sites, which favors the adsorption of nucleophilic NO_3^- (Fig. 4(b)) [23]. Furthermore, charge transfer analysis confirmed the transfer of 0.62 electrons from the Co atom to the NO_3^- moiety, suggesting that the Co site acts as the active center for the NITRR (Fig. 4(c)).

Gibbs free energy calculations along the NITRR pathway provided deeper insights into the reaction mechanism (Fig. 4(d) and Fig. S21). The adsorption of NO_3^- at the Co site was followed by protonation to form *HNO_3, requiring 0.78 eV of free energy. The subsequent conversion of *HNO_3 to *NO_2 was exothermic, releasing 5.18 eV of free energy and producing the first H_2O molecule. The step from *NO_2 to *HNO_2 was endothermic, with a free energy increase of 0.56 eV, marking it as the potential-determining step (PDS). Subsequently, two configurations of *NO adsorption along the N-end and O-end pathways were investigated. Although the O-end configuration exhibited stronger binding (ΔG = –8.50 eV) compared to the N-end configuration (ΔG = –8.25 eV), the hydrogenation of *NO in the O-end pathway required significantly more energy (1.17 eV) than the N-end pathway (0.55 eV). Thus, the N-end pathway was identified as the more favorable route. Further steps involved the reduction of *NO to *N, releasing the third H_2O molecule, followed by the sequential hydrogenation of *N to NH_3, both of which were exothermic. The final desorption of NH_3 completed the catalytic cycle. Additionally, the weaker binding strength of H^+ (ΔG_{*H} = 0.78 eV) compared to NO_3^- at the Co site (Fig. S22) further confirmed the preference for the NITRR over the competing HER process. These findings underscore the excellent electrocatalytic NITRR performance of the Co_2-CRMC cluster, attributed to its strong NO_3^- adsorption capability and the reduced energy barrier for *NO hydrogenation.

Based on the *in-situ* differential electrochemical mass spectrometry (DEMS) analysis, the detection of reaction intermedi-

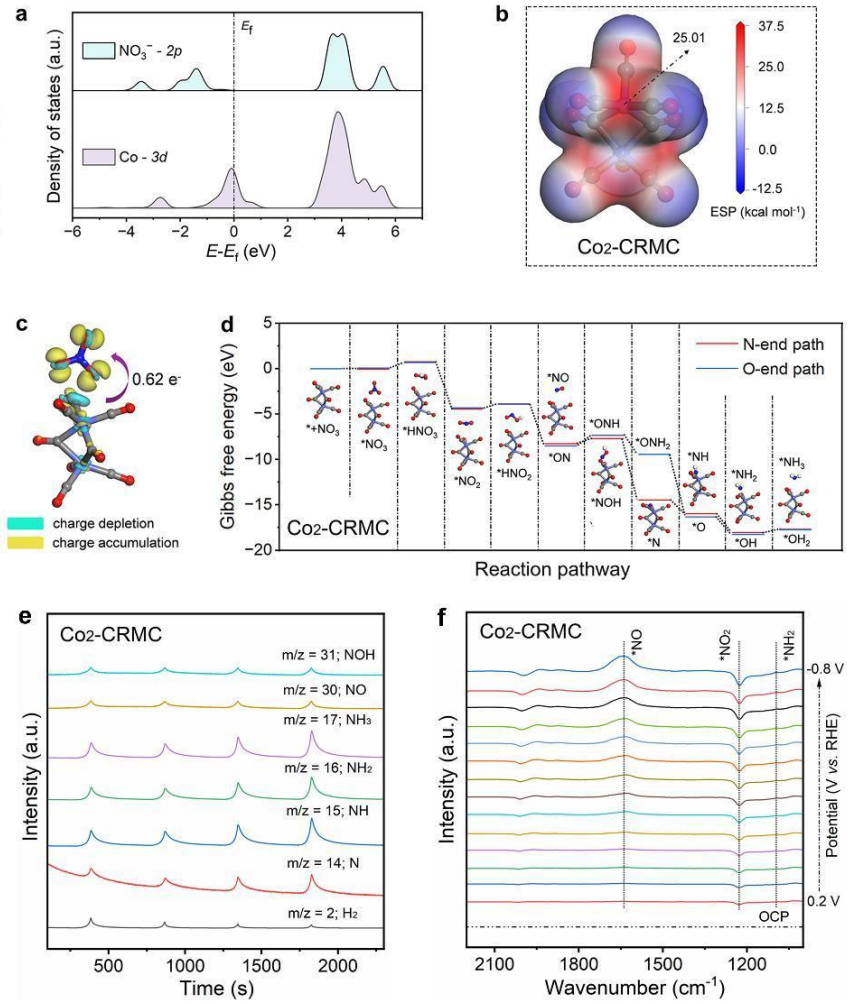

Fig. 4. Theoretical calculations and mechanism studies. (a) The PDOS analysis of Co-3*d* and NO_3^--2*p* adsorbed on the carbonyl-rich Co_2-CRMC model. (b) The ESP surface analysis of the Co_2-CRMC model. (c) The charge density difference of the NO_3^- adsorbed on the Co_2-CRMC model. The cyan and yellow regions corroborate charge depletion and charge accumulation, respectively. The isosurface value is 0.03 eV Å^{-3}. (d) Calculated free-energy diagrams of the possible electrocatalytic NITRR pathways on the Co_2-CRMC model. The inserts illustrate the optimized adsorption configurations of various reaction intermediates along the N-end pathway. (e) *In-situ* DEMS patterns of NITRR on Co_2-CRMC electrode. (f) *In-situ* ATR-FTIR spectra of Co_2-CRMC electrode under various applied potentials.

ates such as NOH, NO, NH_3, and NH_2, particularly the emergence of key NH and N intermediates at m/z = 15 and 14, indicates a more favorable reaction pathway proceeding via the N-end route (Fig. 4(e)). This observation is in good agreement with theoretical simulation results. Regarding the *in-situ* ATR-FTIR measurements, distinct absorption bands around 1640, 1230, and 1097 cm^{-1} are identified, corresponding to NO, NO_2, and NH_2 species, respectively, as shown in Fig. 4(f) [53–56]. These findings further support the presence and evolution of NH_2 characteristic intermediate during the NITRR process.

3.5. *Flow cell tests of NITRR*

The implementation of CRMC in the NITRR requires their ability to function effectively under industrially relevant current densities. To assess this capability, a specialized flow cell configuration was designed for electrocatalytic NITRR evaluation (Fig. 5(a)). LSV measurements were conducted using Co_2-CRMC and Co_4-CRMC electrodes in a 0.1 mol L^{-1} Na_2SO_4–0.1 mol L^{-1} KNO_3 mixed electrolyte, as illustrated in Fig. 5(b). Long-term operational stability is another critical parameter for evaluating catalytic performance. A chronoamperometry experiment was performed on the Co_4-CRMC electrode at a fixed potential of −0.6 V (*vs.* RHE) for a duration of 10,800 seconds within the flow cell system (Fig. 5(c)). The current-time (*I-t*) curve revealed a modest decline after roughly two hours, indicating a slight reduction in catalytic activity. The Faradaic efficiency for ammonia synthesis was measured at 91.1% after one hour, increased to 93.5% after two hours, and maintained at approximately 86.9% following 3 h of continuous operation. Generally, the decay in Faradaic efficiency is primarily attributed to a surface conditioning process under high-current operation, potentially involving subtle restructuring of catalytic sites or temporary adsorption of reaction intermediates, a common phenomenon in the electrocatalytic field.

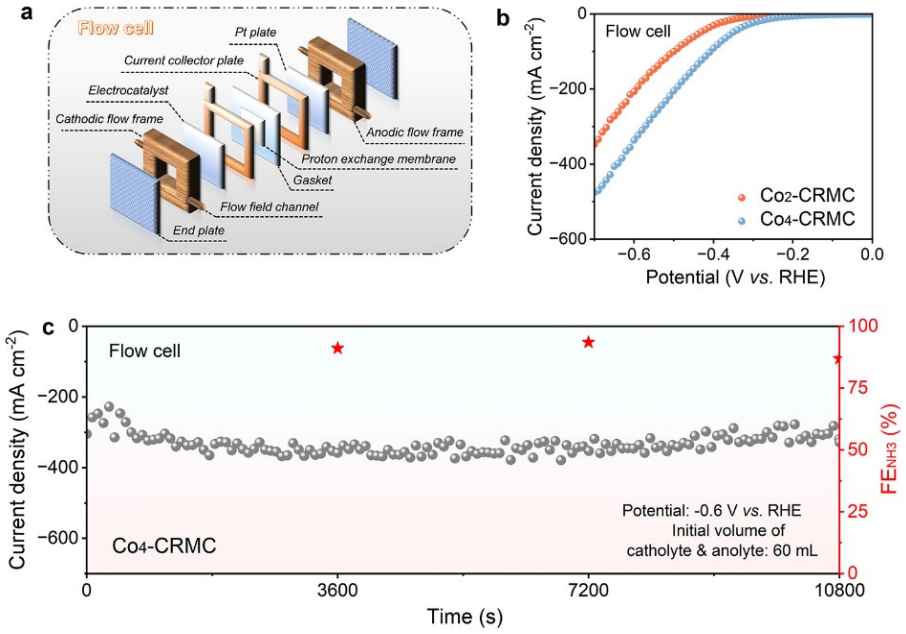

Fig. 5. The NITRR tests in flow cell. (a) Schematic illustration of the flow-cell system. (b) LSV curves of Co_2-CRMC and Co_4-CRMC electrodes tested in 0.1 mol L^{-1} Na_2SO_4–0.1 mol L^{-1} KNO_3 mixed electrolyte. (c) Time-dependent industrially relevant current density curve of Co_4-CRMC electrode at an applied potential of −0.6 V (*vs.* RHE).

4. Conclusions

In summary, we explored atomically precise carbonyl-rich metal clusters as a model platform with exceptional activity and selectivity for direct electrochemical nitrate-to-ammonia conversion in neutral media. To elucidate the intrinsic structure–activity relationship in the NITRR, we conducted a systematic study on various carbonyl-rich metal clusters, such as cobalt (Co_2-CRMC, Co_4-CRMC), ruthenium (Ru_3-CRMC), iron (Fe_2-CRMC, Fe_3-CRMC), molybdenum (Mo-CRMC), tungsten (W-CRMC), and manganese (Mn_2-CRMC) derivatives. Notably, two cobalt-based cluster electrodes demonstrate superior ammonia production performances, achieving near-unity Faradaic efficiencies (~98.0%) under neutral conditions. Theoretical calculations reveal that the high electrocatalytic NITRR performances stem from the preferential adsorption of NO_3^- and the reduced energy barrier for *NO hydrogenation. ESP analyses further highlight the critical role of carbonyl ligands in enhancing the adsorption affinity of Co centers for NO_3^-. This work offers a strategic approach to designing advanced metal cluster catalysts through molecular-level engineering, paving the way for efficient ammonia production and broader applications in sustainable catalysis.

Notes

The authors declare no competing financial interest.

Supplementary materials

Computational details, the crystal structures of carbonyl-rich metal cluster models, SEM, TEM, LSV curves, *I-t* curves, NITRR product selectivity diagram, comparison result of electrocatalytic performance, isotope labeling experiments, CV, EIS, EXAFS fitting curves, fine structure characterizations and electrocatalytic NITRR tests of other carbonyl-rich metal clusters, optimized geometric structures of reaction intermediates, tables of fitted results for the coordination environments of samples, supporting references. Fig. S1–S22 and Table S1–S2.

References

[1] C. Tang, S.-Z. Qiao, *Chem. Soc. Rev.*, **2019**, 48, 3166–3180.
[2] A. Good, *Science*, **2018**, 359, 869–870.
[3] R. Shi, X. Zhang, G. Waterhouse, X. Zhao, R. Zhang, *Adv. Energy Mater.*, **2020**, 10, 2000659.
[4] J. Zhang, X. Tian, M. Liu, H. Guo, J. Zhou, Q. Fang, Z. Liu, Q. Wu, J. Lou, *J. Am. Chem. Soc.*, **2019**, 141, 19269–19275.
[5] L. Hui, Y. Xue, H. Yu, Y. Liu, Y. Fang, C. Xing, B. Huang, Y. Li, *J. Am. Chem. Soc.*, **2019**, 141, 10677–10683.
[6] L. Zhang, L.-X. Ding, G.-F. Chen, X. Yang, H. Wang, *Angew. Chem. Int. Ed.*, **2019**, 58, 2638–2642.
[7] S.-J. Li, D. Bao, M.-M. Shi, B.-R. Wulan, J.-M. Yan, Q. Jiang, *Adv. Mater.*, **2017**, 29, 1700001.
[8] B. Yu, H. Li, J. White, S. Donne, J. Yi, S. Xi, Y. Fu, G. Henkelman, H. Yu, Z. Chen, T. Ma, *Adv. Funct. Mater.*, **2020**, 30, 1905665.
[9] M. Jiang, L. Han, P. Peng, Y. Hu, Y. Xiong, C. Mi, Z. Tie, Z. Xiang, Z. Jin, *Nano Lett.*, **2022**, 22, 372–379.
[10] Q. Gao, H. S. Pillai, Y. Huang, S. Liu, Q. Mu, X. Han, Z. Yan, H. Zhou, Q. He, H. Xin, H. Zhu, *Nat. Commun.*, **2022**, 13, 2338.
[11] C. Liu, G. Zhang, W. Zhang, Z. Gu, G. Zhu, *Proc. Natl. Acad. Sci. USA*, **2023**, 120, e2209979120.
[12] K. C. Majhi, H. Chen, A. Batool, Q. Zhu, Y. Jin, S. Liu, P. H.-L. Sit, J. C.-H. Lam, *Angew. Chem. Int. Ed.*, **2025**, 64, e202500167.
[13] P. H. van Langevelde, I. Katsounaros, M. T. M. Koper, *Joule*, **2021**, 5, 290–294.
[14] Z. Zhang, Y. Lv, Y. Gu, X. Zhou, B. Tian, A. Zhang, Z. Yang, S. Chen, J.

Ma, M. Ding, J.-L. Zuo, *Angew. Chem. Int. Ed.*, **2025**, 64, e202418272.
[15] Y. Wang, M. Sun, J. Zhou, Y. Xiong, Q. Zhang, C. Ye, X. Wang, P. Lu, T. Feng, F. Hao, F. Liu, J. Wang, Y. Ma, J. Yin, S. Chu, L. Gu, B. Huang, Z. Fan, *Proc. Natl. Acad. Sci. U. S. A.*, **2023**, 120, e2306461120.
[16] Z. Song, Y. Liu, Y. Zhong, Q. Guo, J. Zeng, Z. Geng, *Adv. Mater.*, **2022**, 34, 2204306.
[17] S.-E. Bae, K. L. Stewart, A. A. Gewirth, *J. Am. Chem. Soc.*, **2007**, 129, 10171–10180.
[18] S.-J. Zheng, X.-Y. Dong, H. Chen, R.-W. Huang, J. Cai, S.-Q. Zang, *Angew. Chem. Int. Ed.*, **2025**, 64, e202413033.
[19] P. Li, R. Li, Y. Liu, M. Xie, Z. Jin, G. Yu, *J. Am. Chem. Soc.*, **2023**, 145, 6471–6479.
[20] S. Liang, X. Teng, H. Xu, L. Chen, J. Shi, *Angew. Chem. Int. Ed.*, **2024**, 63, e202400206.
[21] L. Liu, S.-J. Zheng, H. Chen, J. Cai, S.-Q. Zang, *Angew. Chem. Int. Ed.*, **2024**, 63, e202316910.
[22] G. Ma, F. Sun, L. Qiao, Q. Shen, L. Wang, Q. Tang, Z. Tang, *Nano Res.*, **2023**, 16, 10867–10872.
[23] R. Zhang, H. Hong, X. Liu, S. Zhang, C. Li, H. Cui, Y. Wang, J. Liu, Y. Hou, P. Li, Z. Huang, Y. Guo, C. Zhi, *Angew. Chem. Int. Ed.*, **2023**, 62, e202309930.
[24] Q. Yang, Q. Xu, H.-L. Jiang, *Chem. Soc. Rev.*, **2017**, 46, 4774–4808.
[25] L. Jiao, Y. Wang, H.-L. Jiang, Q. Xu, *Adv. Mater.*, **2018**, 30, 1703663.
[26] M. Wang, Y.-R. Meng, W. Xu, T. Shen, Y. Wang, Q. Yu, C. Liu, Y. Gu, Z. Tie, Z. Fan, J.-L. Zuo, J. Su, Z. Jin, *J. Am. Chem. Soc.*, **2025**, 147, 18327–18337.
[27] Y. Xiong, B. Li, Y. Gu, T. Yan, Z. Ni, S. Li, J.-L. Zuo, J. Ma, Z. Jin, *Nat. Chem.*, **2023**, 15, 286–293.
[28] Z. Jiang, Y. Wang, Z. Lin, Y. Yuan, X. Zhang, Y. Tang, H. Wang, H. Li, C. Jin, Y. Liang, *Energy Environ. Sci.*, **2023**, 16, 2239–2246.
[29] J. Su, S. Yuan, H.-Y. Wang, L. Huang, J.-Y. Ge, E. Joseph, J. Qin, T. Cagin, J.-L. Zuo, H.-C. Zhou, *Nat. Commun.*, **2017**, 8, 2008.
[30] Y. Tang, Y. Liu, Y. Xia, F. Zhao, B. Zeng, *Anal. Chem.*, **2023**, 95, 4795–4802.
[31] B. Lan, X. Zhang, Y. Wang, C. Wei, G. Wen, *Carbon*, **2022**, 192, 384–394.
[32] L. Li, D. Li, Q. Bai, Y. Wang, C. Li, Y. Shen, H. Uyama, *Energy Fuels*, **2023**, 37, 16942–16950.
[33] Y.-B. Liu, Y.-N. Wang, H.-M. Lu, S. Liang, B.-L. Xu, Y.-N. Fan, *Chem. Eur. J.*, **2016**, 11, 3159–3164.
[34] M. Wang, S. Li, Y. Gu, W. Xu, H. Wang, J. Sun, S. Chen, Z. Tie, J.-L. Zuo, J. Ma, J. Su, Z. Jin, *J. Am. Chem. Soc.*, **2024**, 146, 20439–20448.
[35] L. Sun, V. Reddu, S. Xi, C. Dai, Y. Sheng, T. Su, A. C. Fisher, X. Wang, *Adv. Energy Mater.*, **2022**, 12, 2202108.
[36] L. Liu, T. Xiao, H. Fu, Z. Chen, X. Qu, S. Zheng, *Appl. Catal. B*, **2023**, 323, 122181.
[37] X. Dai, L. Tian, Z. Liu, W. Xu, Y.-P. Liu, Y. Liu, *ACS Nano*, **2022**, 16, 18398–18407.
[38] J. Wang, C. Cai, Y. Wang, X. Yang, D. Wu, Y. Zhu, M. Li, M. Gu, M. Shao, *ACS Catal.*, **2021**, 11, 15135–15140.
[39] M. Xie, S. Tang, Z. Li, M. Wang, Z. Jin, P. Li, X. Zhan, H. Zhou, G. Yu, *J. Am. Chem. Soc.*, **2023**, 145, 13957–13967.
[40] Y. Yu, C. Wang, Y. Yu, Y. Wang, B. Zhang, *Sci. China Chem.*, **2020**, 63, 1469–1476.
[41] N. Zhang, J. Shang, X. Deng, L. Cai, R. Long, Y. Xiong, Y. Chai, *ACS Nano*, **2022**, 16, 4795–4804.
[42] L. Li, C. Tang, X. Cui, Y. Zheng, X. Wang, H. Xu, S. Zhang, T. Shao, K. Davey, S.-Z. Qiao, *Angew. Chem. Int. Ed.*, **2021**, 60, 14131–14137.
[43] Y. Lv, S.-W. Ke, Y. Gu, B. Tian, L. Tang, P. Ran, Y. Zhao, J. Ma, J.-L. Zuo, M. Ding, *Angew. Chem. Int. Ed.*, **2023**, 62, e202305246.
[44] M. Jiang, Q. Zhu, X. Song, Y. Gu, P. Zhang, C. Li, J. Cui, J. Ma, Z. Tie, Z. Jin, *Environ. Sci. Technol.*, **2022**, 56, 10299–10307.
[45] H. Hu, R. Miao, F. Yang, F. Duan, H. Zhu, Y. Hu, M. Du, S. Lu, *Adv. Energy Mater.*, **2024**, 14, 2302608.
[46] G.-F. Chen, Y. Yuan, H. Jiang, S.-Y. Ren, L.-X. Ding, L. Ma, T. Wu, J. Lu, H. Wang, *Nat. Energy*, **2020**, 5, 605–613.
[47] B. P. Chaplin, J. R. Shapley, C. J. Werth, *Catal. Lett.*, **2009**, 130, 56–62.
[48] Z.-Y. Wu, M. Karamad, X. Yong, Q. Huang, D. A. Cullen, P. Zhu, C. Xia, Q. Xiao, M. Shakouri, F.-Y. Chen, J. Y. Kim, Y. Xia, K. Heck, Y. Hu, M. S. Wong, Q. Li, I. Gates, S. Siahrostami, H. Wang, *Nat. Commun.*, **2021**, 12, 2870.
[49] Z. Gao, Y. Lai, Y. Tao, L. Xiao, L. Zhang, F. Luo, *ACS Cent. Sci.*, **2021**, 7, 1066–1072.
[50] Y. Wang, W. Zhou, R. Jia, Y. Yu, B. Zhang, *Angew. Chem. Int. Ed.*, **2020**, 59, 5350–5354.
[51] R. Zhang, X. Ma, S. Zhang, H. Cui, C. Li, Y. Wang, Q. Li, C. Peng, Y. Guo, C. Zhi, *Angew. Chem. Int. Ed.*, **2025**, 64, e202507724.
[52] A. Aminu, B. M. Pirzada, S. H. Talib, J. Shaya, I. Yildiz, S. Mohamed, A. Qurashi, *Nano Res. Energy*, **2025**, 4, e9120161.
[53] S. Tang, M. Xie, S. Yu, X. Zhan, R. Wei, M. Wang, W. Guan, B. Zhang,

Graphical Abstract

Chin. J. Catal., 2026, 88: 259–268 doi: 10.1016/S1872-2067(26)65146-7

Direct electrosynthesis of ammonia from nitrate reduction using atomically precise carbonyl-rich metal clusters in neutral media

Miao Wang, Tianyu Shen, Heng Zhou, Shuaikang Yang, Fengkun Hao, Chaohui Wang, Mohan Kumar, Zuoxiu Tie *, Shuangming Chen *, Zhanxi Fan *, Zhong Jin *
Nanjing University, China;
City University of Hong Kong, China;
University of Science and Technology of China, China;
PES Institute of Technology and Management, India

Co-CRMC catalysts achieve ~98% FE in neutral nitrate-to-ammonia electroreduction. Atomically precise carbonyl-rich metal clusters enhance NO_3^- adsorption and lower *NO hydrogenation barriers. Metal-carbonyl ligand interactions optimize electronic environments, enabling high activity and selectivity. This study offers a molecular-level understanding for the design of other metal-cluster catalysts.

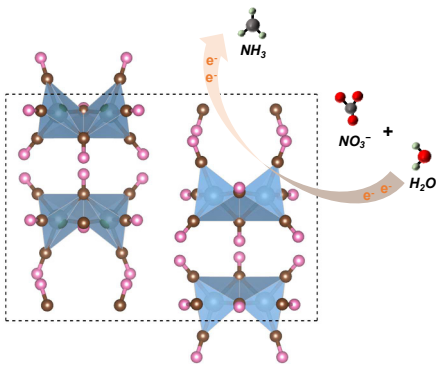

Atomically precise carbonyl-enriched metal cluster

Y. Wang, H. Zhou, G. Zheng, Y. Liu, J. H. Warner, G. Yu, *Nat. Commun.*, **2024**, 15, 6932.
[54] Y. Ma, L. Guo, L. Chang, W. Guo, T. Zhou, F. Hao, W. Su, J. Zhou, G. Wang, M. Shao, J. Yu, J. Yin, Y. Wang, F. Liu, A. Zhang, K. Qian, J. Wang, X. Zhang, W. Zhou, S. Chu, C. Ling, L. Gan, Z. Guo, Z. Fan, *Nat. Commun.*, **2025**, 16, 7632.
[55] S. Han, H. Li, T. Li, F. Chen, R. Yang, Y. Yu, B. Zhang, *Nat. Catal.*, **2023**, 6, 402–414.
[56] Y. Huang, C. He, C. Cheng, S. Han, M. He, Y. Wang, N. Meng, B. Zhang, Q. Lu, Y. Yu, *Nat. Commun.*, **2023**, 14, 7368.

中性介质中利用原子级精准富羰基金属团簇直接电催化还原硝酸盐合成氨

王　淼[a,b,1], 沈天宇[a,1], 周　恒[c,1], 杨帅康[a], 郝风坤[b], 王超辉[b], Mohan Kumar[d], 铁祚庶[a,*], 陈双明[c,*], 范战西[b,*], 金　钟[a,*]

[a]南京大学化学化工学院, 绿色化学与工程研究院, 天长新材料与能源技术研究中心, 苏州新能源材料与器件绿色智能制造重点实验室, 江苏省先进有机材料重点实验室, 高分子高性能材料与技术创新引智基地, 介观化学教育部重点实验室, 配位化学国家重点实验室, 江苏南京210023, 中国
[b]香港城市大学香港清洁能源研究院, 国家贵金属材料工程技术研究中心香港分中心, 香港九龙999077, 中国
[c]中国科学技术大学, 国家同步辐射实验室, 中国科学院纳米科学卓越中心, 安徽合肥230029, 中国
[d]PES理工与管理学院, 卡纳塔克邦希瓦莫加, 印度

摘要: 氨(NH_3)是化学工业的基石, 在氮肥生产中发挥着至关重要的作用, 并正在成为一种前景广阔的富氢能源载体. 然而, 传统的哈伯-博斯法合成NH_3需要在高温高压的极端条件下进行, 其能耗约占全球总能耗的1.5%, 并贡献了全球1.0%–2.0%的二氧化碳排放量. 电化学合成氨为替代哈伯-博斯法提供了一种可持续且环境友好的途径. 硝酸盐作为一种高溶解度、低解离能的氮源, 不仅在全球储量丰富, 还是一种重要的环境污染物, 因此将其转化为氨既具有实际意义, 又有利于环境修复. 利用电驱动的硝酸盐还原合成氨, 为应对环境污染和同步生产高价值氨提供了一种可持续的解决方案. 硝酸盐还原反应过程涉及八个电子和九个质子的转移, 需要大量活性氢(H)的供应. 活性位点处H供应不足常导致副反应发生, 降低法拉第效率和氨产率. 此外, 竞争性的析氢反应进一步复杂化, 因为H*复合生成H_2会分流用于产氨的电子. 因此, 设计具有优化活性位点的电催化剂至关重要.

催化剂主要设计理念是需要高效解离水以生成H*, 同时防止H*复合, 从而确保高的氨选择性和产率. 基于此, 具有明确结构的原子级精准金属团簇, 为研究和优化这些过程提供了一个极具前景的平台. 根据*d*带中心理论, *d*带中心上移可强化金属位点与吸附物之间的相互作用, 从而提升催化活性. 引入吸电子官能团作为配体可以调控*d*带中心, 改善吸附和质子耦合电子转移能力. 这些见解凸显了分子工程金属团簇作为高性能硝酸盐还原反应电催化剂的潜力, 有助于建立内在的构效关系. 本研究探索了富羰基金属团簇(CRMC)作为研究活性位点构型和硝酸盐还原反应机理的模型平台. 我们系统研究了一系列CRMC, 包括Co_2-CRMC, Co_4-CRMC, Ru_3-CRMC, Fe_2-CRMC, Fe_3-CRMC, Mo-CRMC, W-CRMC和Mn_2-CRMC, 以阐明它们在硝酸盐还原反应中的结构-性能关系. 其中, Co_2-CRMC和Co_4-CRMC团簇表现出优异的产氨性能, 在中性水介质中实现了约98.0%的法拉第效率. 理论计算和机理研究表明, 其高催化活性源于对NO_3^-的优先吸附以及*NO加氢步骤的能垒降低. 而静电势分析进一步表明, 羰基配体增强了金属中心的亲核性, 促进了NO_3^-反应物的吸附和后续反应. 根据原位微分电化学质谱分析, 检测到NOH, NO, NH_3和NH_2等反应中间体, 特别是m/z = 15和14处关键NH与N中间体的出现, 表明反应更倾向于通过N端路径进行. 该观测结果与理论模拟高度吻合. 在原位衰减全反射傅里叶变换红外光谱测试中, 观察到1640, 1230和1097 cm^{-1}附近的特征吸收峰, 分别对应NO, NO_2和NH_2物种. 这些发现进一步证实了硝酸根还原反应过程中NH_2特征中间体的存在及其动态演变.

综上, 本文关于原子级精准金属团簇的电催化硝酸根还原方面的研究, 为探索其他基于配位的催化体系(如金属-有机框架、共价有机框架和分子电催化剂)提供了新范式, 也为可持续催化开辟了新途径.

关键词: 富羰基金属团簇; 原子级精准结构; 电化学硝酸盐还原; 电合成氨; 密度泛函理论计算

收稿日期: 2025-11-12. 接受日期: 2026-02-05. 上网时间: 2026-09-05.

*通讯联系人. 电子信箱: zxtie@nju.edu.cn (铁祚庶), csmp@ustc.edu.cn (陈双明), zhanxi.fan@cityu.edu.hk (范战西), zhongjin@nju.edu.cn (金钟).
[1]共同第一作者.

基金来源: 国家自然科学基金(U25A20628, 22561160129, 22479074, 22475096); 装备预研教育部联合基金(8091B02052407); 江苏省基础研究计划重点项目(BK20253008); 江苏省科技重大专项(BG2024013); 江苏省科技成果转化专项资金(BA2023037); 江苏省学位与研究生教育教学改革项目(JGKT24_C001); 苏州市关键核心技术揭榜挂帅项目(SYG2024122); 苏州实验室开放研究基金(SZLAB-1308-2024-TS005); 郴州国家可持续发展议程创新示范区省级专项揭榜挂帅项目(2023sfq11, 2025sfq38); 中央高校基本科研业务费专项资金和南京大学国际合作计划(020514380354).